Atmospheric
Chemistry
and Physics
Discussions

Numerical
simulations of
homogeneous
freezing

Haag et al.

Numerical simulations of homogeneous freezing processes in the aerosol chamber AIDA

W. Haag[1], B. Kärcher[1], S. Schaefers[2], O. Stetzer[2], O. Möhler[2], U. Schurath[2], M. Krämer[3], and C. Schiller[3]

[1]Deutsches Zentrum für Luft- und Raumfahrt (DLR), Institut für Physik der Atmosphäre (IPA), Oberpfaffenhofen, Germany
[2]Forschungszentrum Karlsruhe (FZK), Institut für Meteorologie und Klimaforschung (IMK-3), Karlsruhe, Germany
[3]Forschungszentrum Jülich (FZJ), Institut für Chemie und Dynamik der Geosphäre (ICG-1), Jülich, Germany

Correspondence to: W. Haag (Werner.Haag@dlr.de)

Title Page

Abstract	Introduction
Conclusions	References
Tables	Figures

| ◄◄ | ►► |
| ◄ | ► |

Back | Close

Full Screen / Esc

Print Version

Interactive Discussion

© EGU 2002

Abstract

The homogeneous freezing of supercooled H_2SO_4/H_2O aerosols in an aerosol chamber is investigated with a microphysical box model using the activity parameterization of the nucleation rate by Koop et al. (2000). The simulations are constrained by measurements of pressure, temperature, total water mixing ratio, and the initial aerosol size distribution, described in a companion paper (Möhler et al., 2002). Model results are compared to measurements conducted in the temperature range between 194 and 235 K, with cooling rates in the range between 0.5 and 2.6 K min^{-1}, and at air pressures between 170 and 1000 hPa. The simulations focus on the time history of relative humidity with respect to ice, aerosol size distribution, partitioning of water between gas and particle phase, onset times of freezing, freezing threshold relative humidities, aerosol chemical composition at the onset of freezing, and the number of nucleated ice crystals. The latter three parameters can directly be inferred from the experiments, the former three aid in interpreting the measurements. Sensitivity studies are carried out to address the relative importance of uncertainties of basic quantities such as temperature, H_2O mixing ratio, aerosol size spectrum, and deposition coefficient of H_2O molecules on ice. The ability of the numerical simulations to provide detailed explanations of the observations greatly increases confidence in attempts to model this process under real atmospheric conditions, for instance with regard to the formation of cirrus clouds or type-II polar stratospheric clouds, provided that accurate temperature and humidity measurements are available.

1. Introduction

Although it remains a subject of debate under which atmospheric conditions homogeneous freezing of supercooled aerosols leads to the formation of cirrus clouds, the relevance of this process has been emphasized in many previous studies (Heymsfield and Sabin, 1989; Sassen and Dodd, 1989; Jensen and Toon, 1992; Heymsfield and

Title Page

Abstract | Introduction

Conclusions | References

Tables | Figures

◄◄ | ►►

◄ | ►

Back | Close

Full Screen / Esc

Print Version

Interactive Discussion

Miloshevich, 1993; Jensen et al., 1998; Lin et al., 1998; Field et al., 2001). It has been shown that the special class of orographic ice clouds predominantly forms at large supersaturations with respect to ice at temperatures below the spontaneous freezing point of pure water ($\sim$ 235 K), and it seems likely that homogeneous freezing of su-
5 percooled solutions is the dominant ice particle formation mechanism for this cloud type, given the large cooling rates of air parcels induced by atmospheric waves. It has been demonstrated that one way to form polar stratospheric ice (type-II) clouds occurs *via* homogeneous freezing of diluted supercooled aerosols composed of H_2O, H_2SO_4, and HNO_3 (Carslaw et al., 1997), although other formation pathways may exist (Peter,
10 1997).

The homogeneous nucleation rates used in previous numerical simulations of cirrus formation were subject to significant changes over the last decade (Jensen and Toon, 1991; Tabazadeh et al., 1997, 2000), with a tendency to predict higher freezing thresholds when more recent laboratory results were used to derive the rates (Koop et al.,
15 1998; Chang et al., 1999; Koop et al., 1999; Bertram et al., 2000; Chen et al., 2000). Recently, it has been shown that the threshold relative humidities for homogeneous freezing of chemically different supercooled aerosols are almost similar, provided the freezing droplets (which may contain different types and amounts of solutes) have the same water activity at a given temperature (Koop et al., 2000).
20 In this work, we present a comprehensive comparison of results from ice nucleation experiments carried out in the aerosol chamber AIDA (Aerosol Interaction and Dynamics in the Atmosphere) of Forschungszentrum Karlsruhe with microphysical simulations of the ice initiation process and the initial growth phase of the ice particles using the APSC (Advanced Particle Simulation Code) developed at Deutsches Zentrum für Luft-
25 und Raumfahrt (DLR). The measurements are described in detail in a companion paper (Möhler et al., 2002), but we recall some features relevant for the comparison, for convenience. The simulations use the activity-based parameterization of the homogeneous nucleation rate as given by Koop et al. (2000).

Despite some effects introduced by the large but finite measuring volume, of which

Title Page

Abstract | Introduction

Conclusions | References

Tables | Figures

◄ | ►►

◄ | ►

Back | Close

Full Screen / Esc

Print Version

Interactive Discussion

special care has to be taken in the model, the AIDA approach to simulate ice formation has a great advantage over airborne measurements: important quantities such as the total water mixing ratio and temperature are obtained with high precision in one volume of air where the phase transition actually takes place. This provides strong constraints
5 for the numerical calculations presented below. In the field, it is very difficult to perform Lagrangian-type flights to be able to describe cloud formation in a similar manner, even in quasi-stationary wave clouds. Thus, in many cases, the resulting uncertainties in the computed relative humidities and other variables render definite conclusions about the nature of the underlying nucleation processes impossible. In other laboratory studies of
10 ice formation, it is very difficult to prepare realistic polydisperse aerosols and dynamical environments, and many experiments have been carried out using constant temperatures and monodisperse, super μm-sized droplets. In the AIDA chamber, the number and size distributions of aerosol particles, cooling rates, relative humidities, temperatures, and pressures are typical for the upper troposphere and lower stratosphere, so
15 that these measurements very closely mimic real atmospheric conditions prevailing in cirrus or polar stratospheric ice clouds.

2. Experiments

Figure 1 depicts the overall evolution of the temperature T (black solid curve) and pressure p (red curve) in the chamber volume, the wall temperature, and the total water
20 volume mixing ratio q (blue curve) taken during a typical freezing experiment. The latter is measured with the Lyman-α hygrometer of the Forschungszentrum Jülich (Fast *In situ* Stratospheric Hygrometer, FISH). The FISH instrument demonstrated its reliability to accurately measure low H_2O concentrations (in the ppm-range) in numerous airborne campaigns (Zöger et al., 1999).
25   The freezing experiments in the AIDA chamber start at homogeneous temperature and relative humidity conditions. The initial relative humidity with respect to ice (RHI) is close to ice saturation, established by coating the chamber walls with water ice before

each experiment. A slight offset is observed between the temperature T of the gas in the chamber volume and the temperature of the chamber walls.

Sulfuric acid particles are added to the chamber at a constant pressure. They quickly equilibrate with the available water vapor, forming liquid H_2SO_4/H_2O solution droplets. In the first 3 hours, T, p, and q remain relatively constant and the aerosol size distribution is slightly modified by Brownian coagulation and wall deposition processes. After 220 min the chamber is cooled by volume expansion *via* controlled pumping. Cooling is adiabatic only in the very first stage of the evacuation phase. During this evacuation of the vessel, T drops several degrees below the wall temperature, which remains constant due to the very large heat capacity of the alumimium vessel walls; see Fig. 1. As will be discussed below, the expansion-cooling allows to achieve high supersaturations with respect to ice, sufficient to induce homogeneous freezing of the strongly supercooled H_2SO_4/H_2O aerosol.

When the pumping is stopped at 240 min, T starts to rise driven by the heat flux from the (warmer) chamber walls until it becomes equal to the wall temperature, indicating that the chamber returns to a thermodynamic equilibrium, as depicted in Fig. 1. Refilling the chamber with dry synthetic air at 320 min leads to a transient warming of the gas. Under nearly constant pressure conditions after 400 min, the chamber equilibrates again.

The FISH measurements show an increase of the H_2O-mixing ratio q during the initial rapid cooling phase. This is a result of a net flux of water vapor from the ice-coated chamber walls into the cooler gas. The molecular flux of H_2O is associated with the heat flux discussed above. During the cooling phase, ice particles are formed from the aerosol, as discussed in Sects. 4 and 5.

The decrease of q after the cooling phase may be caused by sedimentation of large ice particles, by wall impaction, or by inefficient sampling by the FISH inlet (the diameter below which the particle sampling efficiency is near 100% is $\sim 7\,\mu m$). It is currently not possible to estimate the relative importance of these processes in reducing q on the basis of the measurements. Using a simplified parameterization of the apparent loss

Numerical simulations of homogeneous freezing

Haag et al.

of total water, we will return to this issue in more detail in Sect. 4.3.

3. Modeling

In this work, we employ the DLR aerosol/cloud trajectory model APSC, with modules treating the microphysical processes involved in the AIDA experiments. Results of this model obtained during phase 1 of the Global Energy and Water Cycle Experiment (GEWEX) cirrus parcel model intercomparison project are discussed in Lin et al. (2002) and Kärcher and Lohmann (2002). A description of the model physics relevant to the present studies is given below.

We drive the simulations with measured temperature, pressure, total water mixing ratio and initial aerosol size distribution, similar to the case study depicted in Fig. 2. Recall from Möhler et al. (2002) that the expansion cooling becomes non-adiabatic shortly after the onset of pumping. The model solves the equations governing condensational growth of the liquid particles and depositional growth of ice particles by uptake of water vapor. The physical processes are treated kinetically over a moving center size structure (Jacobson, 1999). In the moving center size structure, size-bin edges are fixed, but size-bin centers can change. The particles are allowed to grow or evaporate to their exact sizes. If the average volume of a particle in a bin grows larger than the high-edge volume of the bin, all particles in the bin are moved to a single bin bounding the new average volume. This scheme is almost free of numerical diffusion, because all particles are moved to the same size bin and are not partitioned amongst two or more size bins.

Aerosol and ice particles are treated as separate particle types. The aerosol and ice particle size distrubutions are discretized over 80 size bins with a constant bin-volume ratio of 1.6, starting at a minimum particle radius of 1 nm. It is important to use a fine size grid in order to simulate the freezing process precisely. The constant time step chosen is $\Delta t = 0.1$ s, sufficiently small to yield accurate numerical solutions. The initial size distribution of the aerosol particles is lognormal, with dry H_2SO_4 mass, mean

Numerical simulations of homogeneous freezing

Haag et al.

Title Page

Abstract	Introduction
Conclusions	References
Tables	Figures

◀◀　　　▶▶

◀　　　▶

Back　　　Close

Full Screen / Esc

Print Version

Interactive Discussion

mass radius, and geometric standard deviation σ as input parameters. As we are only interested in the growth of freshly nucleated, small (up to several μm) ice particles, the assumption of a spherical shape is reasonable.

Growth and evaporation of aerosols are treated using the analytical predictor of dissolution (APD) scheme introduced by Jacobson (1999). This scheme is non-interative, unconditionally stable, mass-conserving, and fully coupled to the gas phase. In the APD scheme, the size-resolved mass concentrations of all chemical components in the aerosol and ice particles and their respective concentrations in the gas phase are tracked as a function of time. (In the current simulation, only H_2O is allowed to change.) A measure of the mass concentration is the mass fraction, that is the mass of a given species in a particle divided by the total particle mass. Note that the H_2SO_4 mass fraction W in an aerosol particle depends on the particle size due to the Kelvin effect. The bulk phase vapor pressure of water is taken from Luo et al. (1995). The Kelvin term enhances this pressure significantly for particles with radii below about $0.05\,\mu$m. Coagulation processes are switched off in the simulations, as they are too slow to affect the freezing process and the growth of the pristine ice particles. (This cooling and growth phase lasts only about 30 min.) We define a constant loss of liquid H_2SO_4/H_2O particles in the simulations, corresponding to the observed decrease of the total number concentration of aerosol particles at constant pressure conditions in the AIDA chamber due to particle sedimentation and diffusional losses to the chamber walls.

With regard to freezing, we use the homogeneous nucleation rates J measured and parameterized by Koop et al. (2000). In this formulation, J depends only on T and on the water activity $a(W, T)$ of the aerosol particles, which, in turn, is size-dependent. The principal features of cirrus formation driven by adiabatic cooling based on these measurements have been discussed elsewhere (Kärcher, 2002; Lin et al., 2002). At each time step and in each size bin, we calculate the nucleation time scale $t_{nuc} = 1/(V J)$, where V is the particle volume, and compare it with the time step Δt. The fraction of freezing aerosol particles in each time step is thus proportional to $\exp\left(-\Delta t/t_{nuc}\right)$. This method allows partial freezing in each aerosol size bin and conserves the total mass

Numerical simulations of homogeneous freezing

Haag et al.

Full Screen / Esc

Print Version

Interactive Discussion

of each chemical species.

Growth and evaporation of ice crystals are treated using the analytical predictor of condensation (APC) scheme introduced by Jacobson (1999). This scheme is similar to the APD scheme, but the vapor pressure here is only a function of temperature.

5   We emphasize that it is of great importance to accurately simulate the relative humidity in the chamber volume in any study of freezing nucleation. As discussed with the help of Fig. 1, the total H_2O mixing ratio varies as a function of time due to interactions between the gas phase and the ice-coated walls. Independent measurements of the H_2O concentration in the gas phase are not available. The question arises how to
10   consider these wall effects in the model.

We constrain our simulations with the measured total water mixing ratios, but calculate the time-dependent partitioning of H_2O between the gas phase, the aerosol phase, and the ice phase explicitly. At each time step, we increase the model gaseous H_2O mixing ratios corresponding to the increase of the FISH data during the cooling phase,

15   $$H_2O(total)_{FISH} \uparrow \quad \longrightarrow \quad H_2O(gas)_{model} \uparrow ,$$

and remove the model ice water corresponding to the decrease of the FISH data after freezing

$$H_2O(total)_{FISH} \downarrow \quad \longrightarrow \quad H_2O(ice)_{model} \downarrow .$$

In this manner, both, H_2O fluxes from the chamber walls (increasing q) and losses of
20   ice water (decreasing q) are implicitly taken into account, removing uncertainties in the simulated time history of relative humidity. Recall the reasons for the loss of ice water after the cooling phase: sedimentation of large crystals; particle losses caused by impaction on the chamber walls or on the mixing fan; undersampling of large crystals by the FISH instrument. We decrease the model ice water content by subtracting the
25   value $q(t) - q(t + \Delta t) \geq 0$ starting from the ice mass present in largest size bins of the ice crystals at each time step. Of course, this removal of ice mass in the model is not intended to be a realistic calculation of the above-mentioned ice water losses.

Numerical simulations of homogeneous freezing

Haag et al.

Title Page

Abstract	Introduction
Conclusions	References
Tables	Figures

◄◄	►►
◄	►
Back	Close

Full Screen / Esc

Print Version

Interactive Discussion

The degree to which remaining uncertainties caused by the precision and accuracy of the FISH and temperature measurements affect the simulation results are addressed in Sect. 6, along with other sensitivity studies. We note, however, that the decrease of q after the cooling phase is not relevant for our study, as the freezing process is terminated while q is still increasing.

4. Case study at 202 K

We analyze in detail a cooling event starting at 202 K and an initial pressure of 180 hPa (experiment A3_1 as noted in the companion paper); see Fig. 2. The total time of the simulation is 40 min, starting 180 s before the chamber cooling.

4.1. Initial aerosol size distribution

The dashed curve in Fig. 3 represents the initial aerosol volume distribution measured in the AIDA chamber with the help of a differential mobility analyser (Möhler et al., 2002). In the APSC simulation, we fit this distribution with a dry mean mass radius of 0.16 μm and a geometric standard deviation of $\sigma = 1.75$ and let the resulting aerosol equilibrate with the available water vapor (green curve). We use these aerosol parameters as baseline values in the model.

Freezing predominantly occurs in the large size portion of the aerosol spectrum, since the homogeneous nucleation probability is proportional to the liquid aerosol volume (Pruppacher and Klett, 1997). Unfortunately, there is only very limited experimental information about particle sizes greater than $\sim 1 \mu$m.

To investigate the influence of the initial aerosol size distribution on the number of nucleated ice particles, we have also run the model with a narrower size distribution ($\sigma = 1.5$, red curve), and a distribution with larger liquid particles ($\sigma = 2$, blue curve). The narrow size distribution is a good representation of measured total particle volume, whereas the broad distribution yields a better fit of the measured total number concen-

Title Page

Abstract	Introduction
Conclusions	References
Tables	Figures

◄◄   ►►

◄   ►

Back   Close

Full Screen / Esc

Print Version

Interactive Discussion

tration of aerosol particles. The results of these sensitivity studies are presented in Sect. 6.

4.2. Relative humidity

The simulated time evolution of RHI is shown in Fig. 4. Initially, gaseous H_2O is in equilibrium with the ice-saturated chamber walls. However, our simulation starts with a RHI of only 90%, because there is a small difference between gas and wall temperature before cooling; see Fig. 2 and refer to Möhler et al. (2002).

While the pressure drop in the chamber reduces the number density of H_2O, the ice saturation pressure drops more rapidly due to the decreasing gas temperature. Thus, cooling of the gas leads to a rapid increase of RHI. For the given conditions, the measurements by Koop et al. (2000) yield an approximate threshold value for homogeneous ice nucleation (RHI_{nuc}) of ∼ 160%. (More precisely, RHI_{nuc} varies from 161% to 157% for freezing droplet radii in the range $0.1\,\mu m$ to $5\,\mu m$.) When this threshold is exceeded around $300\,s$, a fraction of the aerosol particles start undergoing the phase transition. How far the RHI can exceed the critical value depends on the number of ice crystals formed, which in turn depends on T, dT/dt, and aerosol freezing properties. We come back to this issue when discussing Fig. 11.

After the onset of freezing, rapid depositional growth of the nucleated ice crystals lowers the gas phase concentration of H_2O and halts the rise of RHI due to ongoing cooling of the chamber air. (According to Fig. 2, T continues to fall until t = $600\,s$.) Despite the low temperature and the high cooling rate, which both favor larger differences between the peak and the threshold values of RHI, the peak RHI of 165% is only a few percent larger than RHI_{nuc}. When RHI starts falling below RHI_{nuc}, no further ice particles are formed, but depositional growth of the existing ice particles continues. Exchange of H_2O with the aerosol particles does not affect the evolution of RHI significantly, as the water content in the aerosol particles remains small; see Sect. 4.5.

After about $600\,s$, when T begins to rise due to the heat flux from the chamber walls (recall Fig. 2), RHI comes close to 100%. At this time, p is still falling, reducing the

Title Page

Abstract | Introduction

Conclusions | References

Tables | Figures

◀ | ▶|

◀ | ▶

Back | Close

Full Screen / Esc

Print Version

Interactive Discussion

H_2O number density. On the other hand, the FISH data indicate that q rises due to a net molecular flux from the chamber walls. This H_2O flux compensates the pressure-induced decrease of H_2O and re-establishes equilibrium between the moisture in the chamber and the ice-coated chamber walls at the lower pressure, as will be elucidated in Sect. 4.5.

We also ran the model assuming a constant total H_2O mixing ratio (not shown here), i.e. ignoring the observed increase in total water during cooling. These calculations show a continuous fall of RHI to values below 70% after 800 s, in sharp contrast to the measurements. This underlines the importance to constrain such types of simulations with accurate measurements of q and T, which are hard to obtain in airborne field campaigns.

On two occasions near 800 s and near 1400 s, RHI drops slightly below ice saturation (Fig. 4). These drops in RHI are correlated with a smaller pumping speed and therefore with an enhanced temperature increase (recall Fig. 2). The brief undersaturations force the ice particles to evaporate, which tends to establish equilibrium again. The explanation of this subtle detail in the evolution of a highly sensitive quantity such as RHI increases the confidence in the ability of our model to simulate the physics of the freezing and growth processes correctly.

4.3. Particle number concentrations

The simulation starts with a reservoir of 1460 cm^{-3} H_2SO_4 aerosol particles, which is close to the observed total number concentration in the AIDA chamber. The volume expansion *via* pumping causes the aerosol number concentration to decrease; see Fig. 5. Over most of the simulation period, the observed and simulated particle concentrations agree well and closely follow the pressure evolution. At constant pressure conditions before 200 s and after about 1400 s the total number concentration also slightly decreases. This is caused by the loss processes of H_2SO_4/H_2O aerosols in the AIDA chamber (recall Sect. 3).

An exceptional change occurs at 345 sec. At this point, the modeled aerosol num-

ber concentration exhibits a sharp decrease, indicating the transition of the liquid to the ice phase. Freezing occurs within only several tens of seconds, because the occurrence of this sharp decrease coincides with the crossing of the RHI-curve and the RHI_{nuc}-line as shown in Fig. 4. The simulated aerosol concentration drops by about 90

5   particles per cm^3, which is equal to the number of ice particles formed; see Fig. 6. In the experimental data shown in Fig. 5, the drop of the particle concentration cannot be discerned, because the particle counter measures the sum of aerosol and ice particle concentrations (although at later times larger ice particles may not have been detected due to the high-size cut-off of the particle counter and depending on the evaporation

10   rate of the particles in the detection system).

In Fig. 6, we define the onset of freezing at 330 s. A maximum ice number density of $94\,cm^{-3}$ is reached within 20 s. Further nucleation of ice particles is prevented by the fall of RHI below the freezing threshold. The time scale τ of the nucleation event at the freezing temperature of 198 K is inversely proportional to the cooling rate dT/dt, as

15   given by Kärcher and Lohmann (2002):

$$\tau[s] = \left(78.5\,\frac{dT}{dt}[K\,s^{-1}]\right)^{-1}.$$

Inserting the observed cooling rate $dT/dt = 0.012\,K\,s^{-1}$ at 198 K, we obtain $\tau \sim 1\,s$. We have checked that this compares well with the full width at half maximum of the size-integrated nucleation pulse $J(t)$, which is $\sim 3\,s$ according to our simulation.

20   In Fig. 7, the simulated ice number density is compared with the AIDA observation. Both, the onset of freezing and the total number density are very well captured by the simulation. The sharp rise in depolarisation of backscattered Ar^+ laser light (red curve) coincides nicely with the detection of particles by the optical particle counter, which is only sensitive to large (ice) particles (Möhler et al., 2002).

25   If we take into account the above-mentioned losses of ice water by empirically relating the simulated ice water content to the observed decrease of the total water mixing ratio (recall Sect. 3), the simulation shows a similar decrease of the ice particle number

Title Page

Abstract   Introduction

Conclusions   References

Tables   Figures

◄◄   ►►

◄   ►

Back   Close

Full Screen / Esc

Print Version

Interactive Discussion

density as the measurements.

4.4. Aerosol size distributions and chemical composition

Figure 8 displays the changes in modeled size distributions at the time of particle freezing. We first discuss the ice particle spectrum in the bottom panel. The first ice particles are seen around 330 s with a mean number diameter near $0.8\,\mu$m. Up to 350 s, the mean size increases only slightly, but the concentration rises by a factor 10^4, indicating slow growth and rapid freezing. Thereafter, freezing is terminated and the ice particles grow to a mean diameter of $2.4\,\mu$m at 380 s, a size range where growth is almost fully controlled by diffusion. As the radial growth rate in the diffusion regime is inversely proportional to the particle size, small particles grow faster than larger ones, creating a relatively narrow size spectrum of pristine ice particles. The separation into rapid freezing and subsequent relatively slower growth supports the interpretation of the measured depolarisation of the backscattered laser light at the time of nucleation, as detailed in Sect. 3.1 of the companion paper (Möhler et al., 2002).

As the aerosol distribution in Fig. 8 (top panel) shows, no freezing of liquid sulfuric acid aerosol particles occurs for diameters larger than $\sim 4\,\mu$m. At first glance, this seems surprising because the homogeneous freezing rate should increase with the particle volume. These largest aerosol particles remain liquid because transport of water vapor to them is limited by diffusion in the gas phase. During the rapid cooling in this experiment, the water activity in the larger particles lags behind the relative humidity. Hence, at the time when freezing of e.g. $1\,\mu$m particles commences, the water content (or water activity) of larger (e.g. $4\,\mu$m) particles is too small and the solution droplets are too acidic to undergo freezing.

This finding is further supported by Fig. 9, showing H_2O mass fractions W as a function of time and particle size. The dotted curve displays the mass fraction distribution at the beginning of the simulation. As long as no freezing occurs, strong condensational growth driven by the increase of relative humidity dilutes the supercooled droplets. At 340 s, W peaks at 75% in $1\,\mu$m-sized droplets. Note that very large droplets with diam-

Title Page

Abstract	Introduction
Conclusions	References
Tables	Figures

◄◄ ►►

◄ ►

Back Close

Full Screen / Esc

Print Version

Interactive Discussion

eters above 20 μm do not take up H$_2$O significantly.

Aerosol particles below 0.1 μm in diameter take up little H$_2$O, too, due to the Kelvin growth barrier. In contrast to the large droplets, the small droplets always stay very close to equilibrium with H$_2$O in the gas phase, and react almost instantaneously to the changes of RHI. Because of the diffusion limitation, the larger aerosol particles evaporate water molecules more slowly when RHI starts to fall after 340 min, as indicated by the humps in the curves shown in Fig. 9 in the diameter range 5 – 10 μm.

4.5. Partitioning of water

As detailed in Sect. 3, all simulations are constrained with measured total water mixing ratios, so that at each time, total water in the model equals its measurement value. Figure 10 shows the modeled partitioning of q into water vapor, liquid (aerosol) water content, and ice water content, which cannot be inferred from the measurements.

Initially, the major part of total water resides in the gas phase, with only little liquid water present in the aerosol. The aerosol water content increases owing to condensational growth of the supercooled droplets before freezing, thereafter it decreases. The zoom of aerosol water content inside Fig. 10 shows a steep decrease between 340 s and 350 s. This part of aerosol H$_2$O is lost by the conversion of a fraction of the aerosol into ice particles (compare with Fig. 6). In contrast, the subsequent slower decrease is caused by the evaporation of H$_2$O molecules from the aerosol with falling RHI; this is the well known fact that ice particles grow at the expense of supercooled droplets if they coexist.

The gaseous H$_2$O reservoir is depleted by deposition onto ice particles after freezing between 300 s and 400 s. This loss of gaseous water on ice is partly compensated by the wall flux of H$_2$O molecules into the gas, as the increasing total water mixing ratio reveals.

At 800 s, a maximum ice water content of almost 11 ppmv is reached. On the other hand, we find a decrease of only $\sim$ 5 ppmv in the gas phase due to deposition on the ice particles. This implies that most of H$_2$O molecules released from the chamber walls

Numerical simulations of homogeneous freezing

Haag et al.

deposit very quickly onto the growing crystals. In fact, the time scale for depletion of the H_2O number density is given by $1/(4\pi D r \beta(r) n) \simeq 25\,s$, evaluated with the diffusion coefficient $D = 0.211\,cm^2\,s^{-1}(1013.25\,hPa/p)(T/273.15\,K)^{1.94} \simeq 0.9\,cm^2\,s^{-1}$, an ice particle radius $r = 1\,\mu m$, the factor $\beta = 0.4$ controlling the transition between kinetic and diffusive growth regime, and the peak ice particle number density $n = 90\,cm^{-3}$. The transitional factor is given by $1/\beta = 1 + 4\lambda/(3\alpha r)$, where $\lambda = 0.53\,\mu m$ is the mean free path of H_2O molecules in air (at 200 K and 180 hPa). The deposition coefficient α is equal to 0.5 in the baseline simulations.

At 800 s and 1400 s, the RHI drops slightly below 100% (recall Fig. 4). This leads to a transient evaporation of the ice particles. In concert with the wall flux, this evaporation leads to an increase of gaseous H_2O (Fig. 10) until the cooling phase is finished.

The dotted curves display the expected behavior of the system in the absence of losses of ice water. The losses (for which potential reasons have been mentioned in Sect. 3) become important after 900 s. While such effects cause the ice water content to decrease much faster than evaporation alone, its impact on the gas phase concentration is very limited as can be seen in Fig. 10. In summary, it is important to note that the partitioning of water shown in Fig. 10 is primarily driven by the H_2O wall flux and the interaction with ice, both controlling the time history of the relative humidity.

5. Experiments in other temperature regions

We present the APSC results with supercooled H_2SO_4/H_2O droplets covering initial temperatures from 194 K to 235 K and cooling rates at the point of freezing in the range $0.5\,K\,min^{-1}$ to $2.6\,K\,min^{-1}$. To obtain lognormal aerosol size spectra at $t = 0$, we have used the measured total H_2SO_4 masses and spectral width and varied the mean mass radii such that model and observed total aerosol number concentrations agreed, except for B4_1 and C1_1, where $\sigma = 1.8$ has been prescribed. In comparing APSC results with the AIDA data, we focus on total ice particle number densities, peak values of supersaturation with respect to ice and freezing threshold values (RHI_{nuc}),

Title Page

Abstract | Introduction

Conclusions | References

Tables | Figures

◀◀ | ▶▶

◀ | ▶

Back | Close

Full Screen / Esc

Print Version

Interactive Discussion

the times of the onset of freezing, and the H_2SO_4 mass fractions (W_{nuc}) in the freezing particles. These values correspond the model output (besides other details of the H_2O partitioning) left unconstrained by experimental data and provide a stringent test of our ability to accurately simulate homogeneous ice formation.

5   5.1.   Supersaturations

Figure 11 compares the modeled values of peak RHI (filled circles) and RHI_{nuc} (open circles) with the observed threshold values for homogeneous ice nucleation in the AIDA chamber (open squares). Shown as a dashed (dotted) curve is the threshold RHI as a function of T for which a particle with radius $0.25\,\mu m$ ($1\,\mu m$) freezes in one second
10 (one minute), derived using the nucleation rate parameterization provided by Koop et al. (2000). Both curves approximately bracket the range of particle sizes and nucleation time scales in the AIDA. In the first case (dashed curve), the critical nucleation rate J and the difference $\Delta a = a - a_i$ between the critical water activity and the activity at ice equilibrium take the value $J = 1.5 \times 10^{13}\,cm^{-3}\,s^{-1}$ and $\Delta a = 0.3204$; in the second
15 case (dotted curve), we find $J = 4 \times 10^9\,cm^{-3}\,s^{-1}$ and $\Delta a = 0.305$.

Comparing the peak values with the freezing thresholds from the model, we observe that the difference between both is of the order of a few percent and tends to increase with decreasing temperature (cases A1_1, A3_1, A5_1). When T falls, ice particle growth rates become slow, allowing RHI to take larger peak values driven by
20 the relatively strong cooling rates prevailing during these experiments. The difference is larger for the highest temperature considered (case C1_1) because the cooling rate was much higher (by a factor $3 - 4$) in this experiment, which compensates the pure temperature effect. These kinetic effects explain why the peak RHI values lie above the dashed and dotted curves that represent onset RHI values given by Koop et al.
25 (2000) that have been derived assuming equilibrium between aerosol particles and water vapor.

With falling T, we also observe an increasing tendency for the onset values to lie above the dashed and dotted curves. This is caused by the non-equilibrium aerosol

Numerical simulations of homogeneous freezing

Haag et al.

Title Page

Abstract	Introduction
Conclusions	References
Tables	Figures

◀◀   ▶▶

◀   ▶

Back   Close

Full Screen / Esc

Print Version

Interactive Discussion

compositions affecting the large aerosol particles ($D > 2\,\mu$m) as discussed in Sect. 4.4. Recall from Fig. 6 that in the model, the onset of ice formation was defined at the time when the number of ice particles exceeded $10^{-3}\,$cm^{-3}. (A similarly low threshold concentration likely determines the experimental onset of ice formation.) The largest particles with such low concentrations would freeze first if they were in equilibrium with the ambient water vapor, but they stay liquid because of their non-equilibrium composition (cp. Figs. 8 and 9). This delays the onset of freezing and caused the RHI$_{nuc}$ values to be higher than the corresponding equilibrium values.

In the atmosphere, kinetic and non-equilibrium effects may occur in cirrus clouds at cooling rates similar to those measured in the AIDA chamber; this has also been found previously on the basis of field measurements (Heymsfield and Miloshevich, 1995).

Apart from two cases A5_1 and C1_1, the modeled and measured RHI$_{nuc}$ values do not differ by more than 3%, which is within the experimental uncertainty of about ±5% (at the lowest temperatures up to ±12%). In the case A5_1, the difference between modeled and measured RHI$_{nuc}$ is probably not real, because this measurement belongs to the very first ones where the uncertainty could be larger than usual (more than ±5 – 12%). Also, the possibility of early freezing caused by heterogeneous freezing artefacts cannot be fully ruled out here (Möhler et al., 2002). The discrepancy seen in the case C1_1 is more difficult to explain. It may be caused by temperature fluctuations of small, turbulent air parcels (eddies) following an adiabatic temperature evolution for short periods of time. Therefore, the formation of ice may have occurred in such eddies at somewhat lower temperatures than the mean gas temperature measured with time resolution of about 3 – 5 s (Möhler et al., 2002). The onset RHI derived with a lower temperature would lead to a higher value, in better agreement with the model result. As a second explanation, the difference could be caused by the larger cooling rate. When the cooling rate is large, RHI$_{nuc}$ becomes sensitive to even small shifts in the freezing onset time.

The threshold RHI$_{nuc}$ from the model lies very close to the (solid) water saturation line. The supercooled droplets become water activated due to the very rapid cooling at

Title Page

Abstract | Introduction

Conclusions | References

Tables | Figures

◀ | ▶

◀ | ▶

Back | Close

Full Screen / Esc

Print Version

Interactive Discussion

the warm temperature and undergo freezing as nearly pure water droplets. It seems that water activation did not occur during this experiment. Under the conditions of case C1_1, large cooling rate and warm temperature, the solution droplets take up great amounts of water and are strongly diluted. This is reflected by the relatively low acid mass fractions of 4.3%. (The APSC yields a value of 16.1% when read off at the time 72 s when the AIDA reports the freezing onset.) Hence, it is interesting to study slight changes of the H_2O vapor pressure parameterization for the nearly pure water droplets, the accuracy of which may be of the order of a few percent or so. If we lower the saturation vapor pressure of water by only 2.5% when the relative humidity exceeds 95% in a sensitivity study, the modeled RHI_{nuc} for case C1_1 is 3.6% lower and also the peak RHI lies just below the water saturation line (see also the model results listed in brackets in Table 1).

5.2. Onset of freezing

In the experiments, the onset time of freezing t_{nuc} is determined by a sharp increase of the depolarisation of an Argon laser beam (Möhler et al., 2002). In the simulations, the freezing onset is defined as the time when the calculated ice number density exceeds 10^{-3} cm^{-3}. Therefore, it is not straightforward to compare the modeled and measured freezing onset times. Nevertheless, as can be seen in Table 1, the model results represent the experimental data very well. The same holds for the APSC and AIDA freezing temperatures T_{nuc} (also listed in Table 1), which can also be inferred from Fig. 11.

The coldest case A1_1 starting at 194.4 K seems to be an exception. Here, t_{nuc} determined in the AIDA is much larger than the modeled value, causing the discrepancy in terms of the cooling rate listed in Table 1. One explanation could be the uncertainty in measuring total water mixing ratio, which can influence the model results (see Sect. 6.1). If we lower the FISH value by 7.5% (model results listed in brackets in Table 1), which is close to the experimental range of uncertainty, the modeled and measured freezing onset times for case A1_1 agree very well again.

5.3. Ice particle fractions

Table 1 also compares modeled and measured peak values of the number density n of ice particles. Except in the case A1_1, where no data are available, the agreement is excellent, demonstrating that the nucleation rate parameterization provided by Koop et al. (2000) can be safely employed to simulate homogeneous ice nucleation. In experiments A1_1, A3_1, and A5_1, the cooling rates increase slightly while the temperature increases by about 18 K, explaining the decrease of n in accord with theory (Kärcher and Lohmann, 2002).

6. Sensitivity analysis

Measured total water mixing ratio, temperature, and initial aerosol size distribution are subject to experimental uncertainties. We focus our sensitivity study on the influence of a variation of these measurement quantities on the modeled total ice particle number density. We also show the sensitivity of our simulations to changes of the deposition coefficient.

6.1. Total water mixing ratio

The total H_2O mixing ratio displayed in Fig. 2 has an accuracy of ±6%. To conservatively evaluate how strong this experimental uncertainty can influence the baseline model run discussed in Sect. 4, we have performed a series of simulations with values 10% higher and lower than the original data, holding all other input parameters constant.

The imposed shifts of the total H_2O mixing ratio by ±10% (top panel of Fig. 12) lead to a variability of the total ice number density of $\sim$ ±80% (bottom panel), slightly more than the experimental uncertainty of the measurement data (recall the vertical bar in Fig. 7). In the absence of ice particles before the freezing process, higher or lower

values of the total water mixing ratio directly increase or decrease the gaseous H_2O in the simulations. Hence, the threshold value of RHI for homogeneous ice nucleation (RHI_{nuc}) is reached earlier or later, as the different freezing onsets in Fig. 12 indicate.

We cannot argue that a higher (lower) total H_2O mixing ratio consistently increases (decreases) the number of nucleated ice particles. Because of the time shifts of the freezing onset times, the aerosol particles undergo the phase transition at different temperatures and cooling rates. In turn, this leads to shifts in the narrow range between the peak RHI and RHI_{nuc}. It is the exact combination of T, dT/dt and RHI around the time where the ice saturation ratio reaches its peak that controls the total number of ice crystals formed. For example, in a model run with a FISH value $+2.5\%$ more ice particles form than in a run with a value $+5\%$ (not shown in Fig. 12). This study underlines the importance to obtain accurate measurements of H_2O mixing ratios for modeling cirrus cloud formation in the real atmosphere.

6.2. Temperature

In modeling ice formation in the AIDA chamber, we assume that the air volume containing the freezing particles is homogeneously mixed. The typical time scale for mixing of the total volume is of the order of a few seconds, short enough to ensure that this assumption should be valid in most of the cases considered. Vertical inhomogeneities in temperature may occur when very high cooling rates are applied, leading to patches of air that contain lower and higher number densities of crystals (compared to a well mixed situation) that subsequently mix. Temperature fluctuations may become important when the cooling rates are very slow, because mixing rates decrease when the temperature is only weakly varying. As the AIDA sensors measure static temperatures, such fluctuations are not included in the model.

We investigate the sensitivity of our simulations upon uncertainties in temperature in two ways. First, we vary the temperature profile by ± 0.3 K according to the experimental accuracy (see top panel of Fig. 13). Second, we shift the time axis of measured temperature (red curve in the top panel of Fig. 13) by -10 s, that means we start

cooling 10 s earlier (see the zoom of temperature inside Fig. 13, blue curve) without a concomitant shift of the air of H_2O pressures. There is an offset in the temperature measurement because the temperature sensors do not react instantenously to temperature changes. This offset increases from −3 s at 1000 hPa to −10 s at 180 hPa.

The imposed temperature shift results in a variability of the ice number density that is within the range of n caused by the shifts of the FISH data or caused by the temperature uncertainty itself (bottom panel of Fig. 13).

6.3. Deposition coefficient

The deposition coefficient α of water molecules onto the ice particles enters the effective diffusion rate of H_2O molecules (Pruppacher and Klett, 1997). The mass growth rate in the kinetic regime is directly proportional to α, while the rate is independent of it in the diffusion regime. In the upper troposphere, the kinetic regime typically applies for submicrometer-sized particles. Small values of α slow the initial mass growth rate of the freshly formed ice crystals.

The reduction of the initial growth rate allows more ice particles to be formed under otherwise unchanged conditions, because the H_2O vapor concentration stays elevated for a slightly longer time (Kärcher, 2002). As discussed with the help of Fig. 8, the mean number radius r of the ice particles up to 350 s is $\sim 0.5\,\mu$m. The characteristic radius controlling the transition between kinetic and diffusive regime is given by $4\lambda/3\alpha \simeq 1.4\,\mu$m, with the mean free path $\lambda = 0.53\,\mu$m (Sect. 4.5). This radius is of the order of r, thus we can expect a sensitivity of our results upon variations of α.

The value of α is 0.5 for the baseline runs, motivated by laboratory studies (Haynes et al., 1992). Table 2 shows the modeled ice number density for the baseline experiment under the assumption of different values of α. As expected, the total number of nucleated ice particles increases as α decreases, and the rise of n becomes pronounced (the baseline value changes by more than a factor of 2) for values $\alpha < 0.2$. For higher values, the sensitivity is much less pronounced. Comparing Table 2 with Table 1, we conclude that changes of α within the range $0.2\cdots1$ suffice to obtain better

Numerical simulations of homogeneous freezing

Haag et al.

fits to the observed ice number densities, if α is considered to be the only uncertain parameter. We have ran the baseline case with $\alpha = 0.05$ and found no combination of T and total $[H_2O]$ within their uncertainty limits that predicted the number of ice particles consistent with the measurements. Thus, the use of values significantly below 0.2 is not supported by this analysis.

6.4. Aerosol size distribution

With regard to the number of nucleated ice particles, aerosol size effects become important when the time scale of the nucleation event is fast compared to the time scale of depositional growth of the pristine ice particles (Kärcher and Lohmann, 2002). Figure 8 indicates slow growth and rapid freezing for the case study in Sect. 4 and therefore aerosol size effects are important in our simulations.

We investigate the influence of the initial aerosol size distribution on the number of nucleated ice particles by a variation of the geometric standard deviation σ (recall Fig. 3). The results are shown in Table 3. The value of $\sigma = 1.75$ is used in the baseline simulations. A broader or narrower size distribution lead to a variation of the ice number density smaller than its experimental uncertainty, indicating a limited sensitivity of our simulations on the aerosol size distribution compared to temperature and humidity uncertainties, in agreement with theory (Kärcher and Lohmann, 2002).

7. Conclusions

Calculated threshold relative humidities for homogeneous ice nucleation, total ice particle number densities, and times of the onset of freezing agree well with the experimental data, provided the calculations are driven by observed temperature and pressure profiles and take into account water vapor and heat fluxes from the chamber walls. A detailed discussion of a case study, including the evolution of the freezing particles and the partitioning of water between gas, aerosol, and ice phase, elucidated the micro-

physical processes at work during cooling and freezing in the AIDA chamber.

A series of sensitivity studies has shown that the number of ice crystals formed is highly sensitive to variations of the temperature and the total water content. In comparison, variations of the initial aerosol spectrum and of the water vapor deposition coefficient have only a limited influence on the calculated properties of the pristine ice particles.

The freezing studies carried out in the AIDA chamber approximate real cirrus cloud formation in the atmosphere and provide stringent tests of numerical models to simulate these processes. The good agreement between measurements and model results demonstrates that the activity parameterization of homogeneous freezing rates provided by Koop et al. (2000) can be safely employed to simulate the formation of cirrus clouds by this process. The threshold values of relative humidity for homogeneous freezing given by Koop et al. (2000), however, may not exactly hold when applied to atmospheric conditions, as enhanced supersaturations caused by rapid cooling and non-equilibrium compositions of the largest liquid particles can lead to somewhat higher values than determined assuming equilibrium conditions.

References

Bertram, A. K., Koop, Th., Molina, L. T., and Molina, M. J.: Ice formation in $(NH_4)_2SO_4 - H_2O$ particles, J. Phys. Chem., 104, 584–588, 2000. 1469

Carslaw, K. S., Peter, Th., and Clegg, S. L.: Modeling the composition of liquid stratospheric aerosols, Rev. Geophys., 35, 125–154, 1997. 1469

Chang, H.-Y. A., Koop, Th., Molina, L. T., and Molina, M. J.: Phase transitions in emulsified HNO_3/H_2O and $HNO_3/H_2SO_4/H_2O$ solutions, J. Phys. Chem. A, 103, 2673–2679, 1999. 1469

Chen, Y., DeMott, P. J., Kreidenweis, S. M., Rogers, D. C., and Sherman, D. E.: Ice formation in sulfate and sulfuric acid aerosol particles under upper tropospheric conditions, J. Atmos. Sci., 57, 3752–3766, 2000. 1469

Field, P. R., Cotton, R. J., Noone, K., Glantz, P., Kaye, P. H., Hirst, E., Greenaway, R. S., Jost, C., Gabriel, R., Reiner, T., Andreae, M., Saunders, C. P. R., Archer, A., Choularton, T., Smith, M., Brooks, B., Hoell, C., Bandy, B., Johnson, D., and Heymsfield, A.: Ice nucleation in orographic wave clouds: Measurements made during INTACC, Q. J. R. Meteorol. Soc., 127, 1493–1512, 2001. 1469

Haynes, D. R., Tro, N. J., and George, S. M.: Condensation and evaporation of H_2O on ice surfaces, J. Phys. Chem., 96, 8502–8509, 1992. 1487

Heymsfield, A. J. and Sabin, R. M.: Cirrus crystal nucleation by homogeneous freezing of solution droplets, J. Atmos. Sci., 46, 2252–2264, 1989. 1468

Heymsfield, A. J. and Miloshevich, L. M.: Homogeneous ice nucleation and supercooled liquid water in orographic wave clouds, J. Atmos. Sci., 50, 2335–2353, 1993. 1468

Heymsfield, A. J. and Miloshevich, L. M.: Relative humidity and temperature influences on cirrus formation and evolution: Observations from wave clouds and FIRE II, J. Atmos. Sci., 52, 4302–4326, 1995. 1483

Jacobson, M. Z.: Fundamentals of Atmospheric Modeling, Cambridge Univ. Press, Cambridge, U. K., 1999. 1472, 1473, 1474

Jensen, E. J. and Toon, O. B.: Homogeneous freezing nucleation of stratospheric solution droplets, Geophys. Res. Lett., 18, 1857–1860, 1991. 1469

Jensen, E. J. and Toon, O. B.: The potential effects of volcanic aerosols on cirrus cloud microphysics, Geophys. Res. Lett., 19, 1759–1762, 1992. 1468

Jensen, E. J., Toon, O. B., Tabazadeh, A., Sachse, G. W., Anderson, B. E., Chan, K. R., Twohy, C. W., Gandrud, B., Aulenbach, S. M., Heymsfield, A. J., Hallett, J., and Gary, B.: Ice nucleation processes in upper tropospheric wave-clouds observed during SUCCESS, Geophys. Res. Lett., 25, 1363–1366, 1998. 1469

Kärcher, B.: Properties of subvisible cirrus clouds formed by homogeneous freezing, Atmos. Chem. Phys., 2, 161–170, 2002. 1473, 1487

Kärcher, B. and Lohmann, U.: A parameterization of cirrus cloud formation: Homogeneous

Numerical simulations of homogeneous freezing

Haag et al.

Title Page

Abstract	Introduction
Conclusions	References
Tables	Figures

◀◀ ▶▶

◀ ▶

Back Close

Full Screen / Esc

Print Version

Interactive Discussion

freezing including effects of aerosol size, J. Geophys. Res., 107, 10.1029/2001JD001429, 2002. 1472, 1478, 1485, 1488

Koop, Th., Ng, H. P., Molina, L. T., and Molina, M. J.: A new optical technique to study aerosol phase transitions: The nucleation of ice from H_2SO_4 aerosols, J. Phys. Chem. A, 102, 8924–8931, 1998. 1469

Koop, Th., Bertram, A. K., Molina, L. T., and Molina, M. J.: Phase transitions in aqueous NH_4HSO_4 solutions, J. Phys. Chem. A, 103, 9042–9048, 1999. 1469

Koop, Th., Luo, B. P., Tsias, A., and Peter, Th.: Water activity as the determinant for homogeneous ice nucleation in aqueous solutions, Nature, 406, 611–614, 2000. 1468, 1469, 1473, 1476, 1482, 1485, 1489, 1499, 1506

Lin, H., Noone, K. J., Ström, J., and Heymsfield, A. J.: Small ice crystals in cirrus clouds: A model study and comparison with in situ observations, J. Atmos. Sci., 55, 1928–1939, 1998. 1469

Lin, R.-F., Starr, D. O. C., DeMott, P. J., Cotton, R., Sassen, K., Jensen, E., Kärcher, B., and Liu, X.: Cirrus parcel model comparison project phase 1: The critical components to simulate cirrus initiation explicity, J. Atmos. Sci., 59, 2305–2329, 2002. 1472, 1473

Luo, B. P., Carslaw, K. S., Peter, Th., and Clegg, S. L.: Vapour pressures of $H_2SO_4/HNO_3/HCl/HBr/H_2O$ solutions to low stratospheric temperatures, Geophys. Res. Lett., 22, 247–250, 1995. 1473

Möhler, O., Stetzer, O., Schaefers, S., Linke, C., Schnaiter, M., Tiede, R., Saathoff, H., Krämer, M., Mangold, A., Budz, P., Zink, P., Schreiner, J., Mauersberger, K., Haag, W., Kärcher, B., and Schurath, U.: Experimental investigations of homogeneous freezing of sulphuric acid particles in the aerosol chamber AIDA, Atmos. Chem. Phys. Discuss., 2, this issue, 2002. 1468, 1469, 1472, 1475, 1476, 1478, 1479, 1483, 1484, 1493, 1506

Peter, Th.: Microphysics and heterogeneous chemistry of polar stratospheric clouds, Annu. Rev. Phys. Chem., 48, 785–822, 1997. 1469

Pruppacher, H. R. and Klett, J. D.: Microphysics of Clouds and Precipitation, Kluwer Acad. Pub., Dordrecht, 1997. 1475, 1487

Sassen, K. and Dodd, G. C.: Haze particle nucleation simulation in cirrus clouds and application for numerical and lidar studies, J. Appl. Sci., 46, 3005–3014, 1989. 1468

Tabazadeh, A., Jensen, E. J., and Toon, O. B.: A model description for cirrus cloud nucleation from homogeneous freezing of sulfate aerosols, J. Geophys. Res., 102, 23 845–23 850, 1997. 1469

Numerical simulations of homogeneous freezing

Haag et al.

Print Version

Interactive Discussion

Tabazadeh, A., Martin, S. T., and Lin, J.-S.: The effect of particle size and nitric acid uptake on the homogeneous freezing of aqueous sulfuric acid particles, Geophys. Res. Lett., 27, 1111–1114, 2000. 1469

Zöger, M., Afchine, A., Eicke, N., Gerhards, M.-T., Klein, E., McKenna, D. S., Mörschel, U., Schmidt, U., Tan, V., Tuitjer, F., Woyke, T., and Schiller, C.: Fast in situ stratospheric hygrometers: A new family of balloon-borne and airborne Lyman-α photofragment fluorescence hygrometers, J. Geophys. Res., 104, 1807–1816, 1999. 1470

5

Numerical simulations of homogeneous freezing

Haag et al.

Title Page

Abstract	Introduction
Conclusions	References
Tables	Figures

◄◄ ►►

◄ ►

Back Close

Full Screen / Esc

Print Version

Interactive Discussion

Table 1. Simulated freezing experiments with initial temperature T_0 and cooling rate $(dT/dt)_{nuc} = \gamma$. The cooling rates are determined at the times of the freezing onset. Assuming adiabatic cooling, these values would correspond to vertical velocities of the order $120\,\mathrm{cm\,s^{-1}}$, typical for convective updrafts or strong lee waves. The AIDA experiment numbers shown in the first column are taken from Möhler et al. (2002). Further, modeled and measured onset times of freezing t_{nuc}, freezing temperatures T_{nuc}, and H_2SO_4 mass fractions W_{nuc} at t_{nuc} are listed. The onset times now refer to the beginning of chamber pumping to compare with Table 2 from Möhler et al. (2002). The non-equilibrium acid mass fractions are calculated for particles with a diameter of $1\,\mu$m, the observed values are derived from filter measurements assuming water equilibrium. The last two columns compare modeled and measured peak values of total ice particle number density n, including the experimental uncertainty of $\pm 50\%$. The APSC results for case A1_1 listed in brackets represent a model run with a total H_2O mixing ratio lowered by a value of 7.5% (discussed in Sect. 5.2). The results listed in brackets for case C1_1 show the effect of lowering the saturation vapor pressure of H_2O above 95% relative humidity by 2.5% (discussed in Sect. 5.1)

AIDA	T_0[K]	APSC γ [K min⁻¹]	AIDA γ [K min⁻¹]	APSC t_{nuc} [s]	APSC W_{nuc} [%]	APSC T_{nuc} [K]	AIDA t_{nuc} [s]	AIDA W_{nuc} [%]	AIDA T_{nuc} [K]	APSC n [cm⁻³]	AIDA n [cm⁻³]
A1_1	194.4	−0.72	0.09	190	27.0	189.9	270	22.2	189.4	90	no data
		(−0.06)		(268)	(27.1)	(189.4)				(41)	
A3_1	202.2	−0.78	−0.57	150	24.8	197.8	160	22.6	197.6	94	108 ± 54
A5_1	212.6	−0.9	−0.88	152	21.2	208.0	127	23.3	208.2	34	42 ± 21
B4_1	225.9	−0.48	−0.43	268	13.4	220.7	261	15.2	220.7	20	8 ± 4
C1_1	235.3	−2.58	−2.75	96	4.3	230.2	72	16.2	231.0	346	≥ 40
		(−2.58)		(91)	(3.9)	(230.4)				(245)	

Table 2. Sensitivity of simulated ice number density to variations of the deposition coefficient of AIDA experiment A3_1 with initial temperature $T_0 = 202.2$ K

α	0.05	0.1	0.2	0.5	1.0
n [cm^{-3}]	549	278	171	94	61

Table 3. Sensitivity of simulated ice number density of AIDA experiment A3_1 (T_0 = 202.2 K) to variations of the geometric standard deviation σ of the initial aerosol size distribution

σ	1.3	1.5	1.75	2.0
n [cm^{-3}]	74	53	94	74

Numerical simulations of homogeneous freezing

Haag et al.
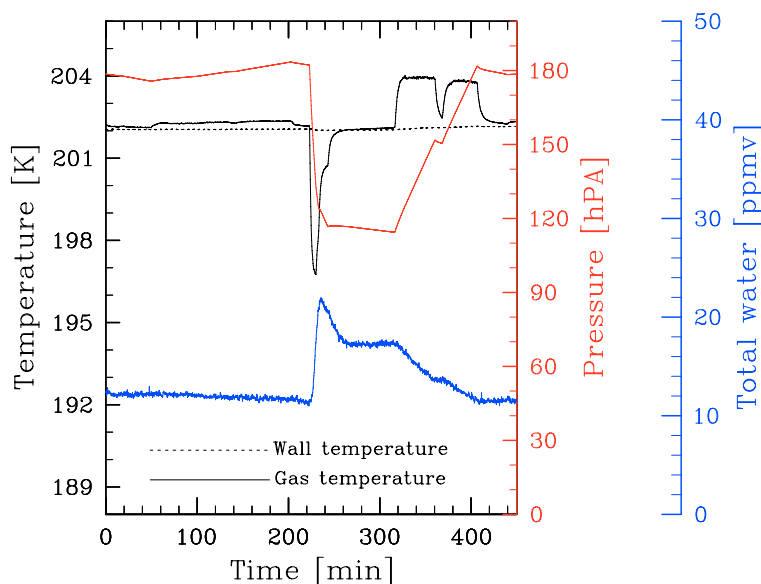
Fig. 1. Variation of pressure, gas and wall temperature, and total water inside the AIDA chamber during a typical freezing experiment. The time scale starts with the generation of binary H_2SO_4/H_2O aerosol. In the period from 220 min to 240 min the fast pressure drop leads to a rapid decrease of the gas temperature, a strong supersaturation with respect to ice, and the initiation of spontaneous freezing of the supercooled aerosols by homogeneous ice nucleation. The variation of total water indicates that H_2O interacts with the chamber walls.
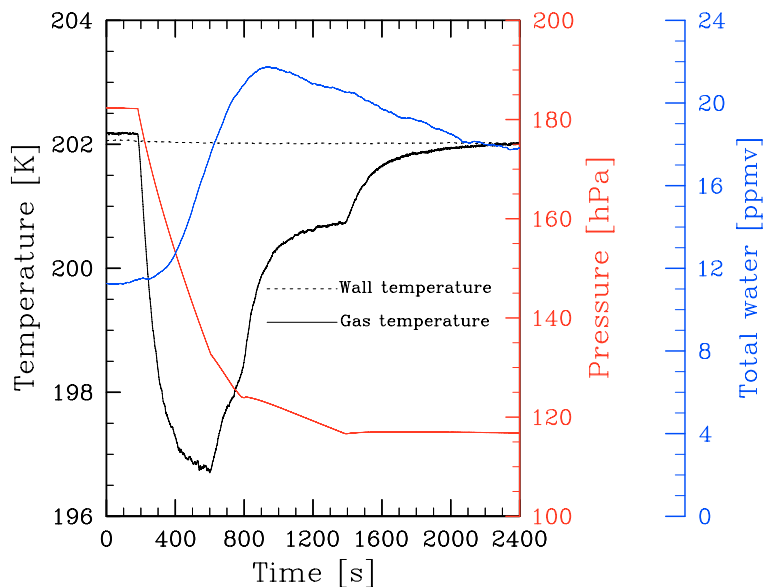
Fig. 2. Modeled cooling period of the case study starting at $T = 202$ K, $p = 180$ hPa, and $q = 11$ ppmv. The wall temperature (dotted curve) varies only slightly. These curves are extracted from Fig. 1 by converting the time units from min to s and by shifting the time axis; pumping now starts after 180 s.

Numerical simulations of homogeneous freezing

Haag et al.
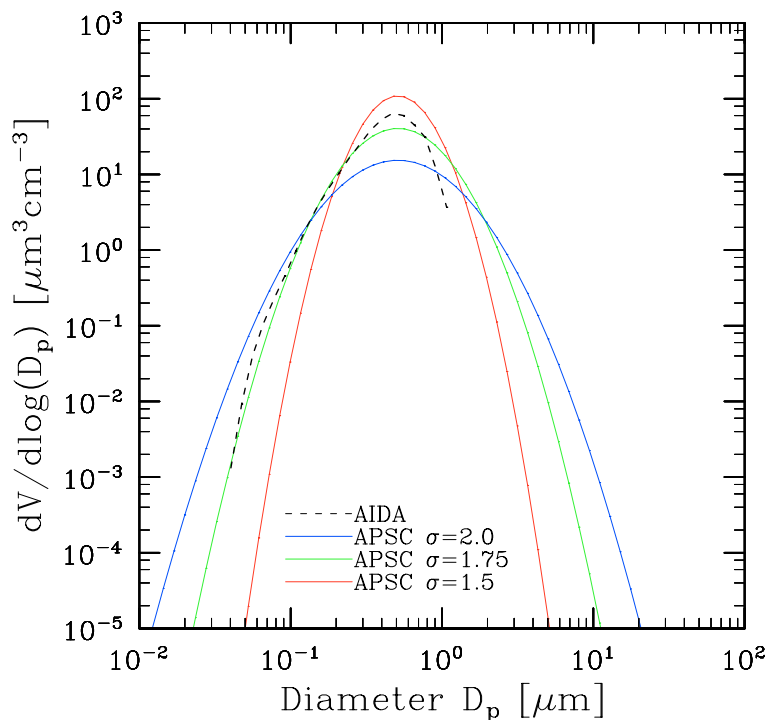
Fig. 3. Wet initial aerosol volume size distributions for the case study shown in Fig. 2. The solid curves represent model fits to the AIDA measurement represented by the dashed curve. The green curve is used in the baseline simulations.
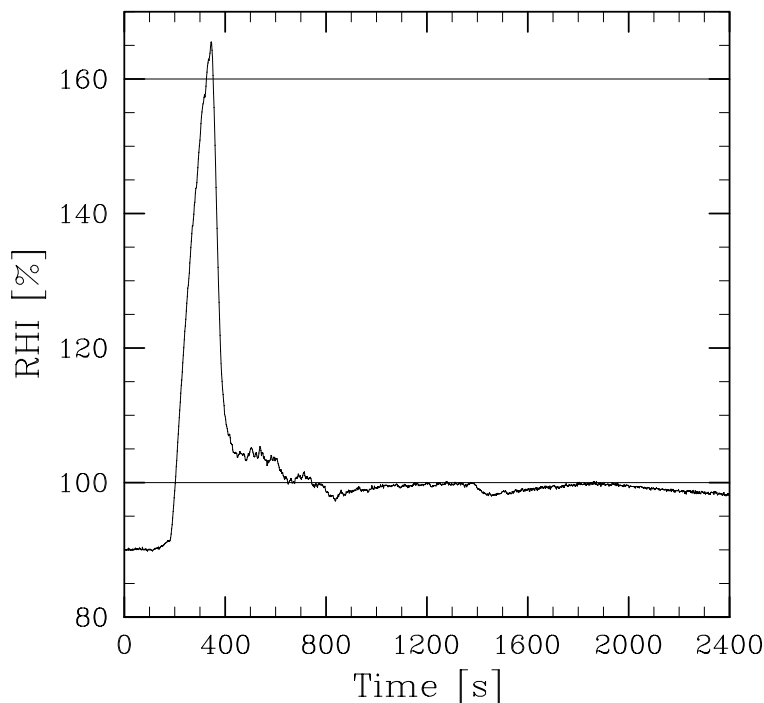
Fig. 4. Modeled relative humidity with respect to ice. The horizontal line at 160% indicates the critical supersaturation for homogeneous ice nucleation at a temperature of 198 K for particles with a radius of $\sim 0.2\,\mu$m (Koop et al., 2000); the corresponding freezing temperature is defined in Fig. 6. The RHI reaches a peak value of 165%.
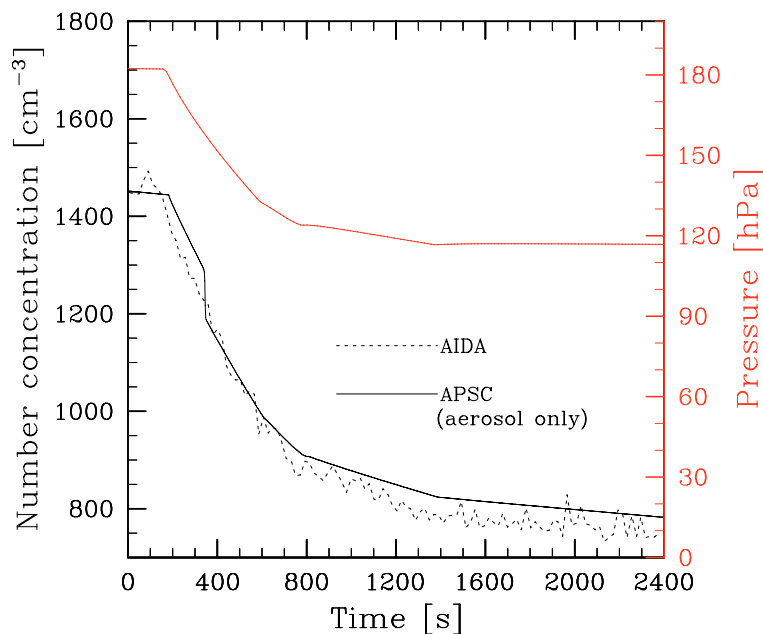
Fig. 5. Pressure and total number concentrations of particles in the chamber versus time. The dashed curve depicts the aerosol measurements (sum of concentrations of aerosol and ice particles in the diameter range 20 nm to 3 μm). In the simulation (solid curve, aerosol particles only), freezing of a small fraction of the aerosol particles is indicated by the sharp decrease at 345 s. During the most of the time, the total particle number concentration closely follows the observed pressure drop (red curve).
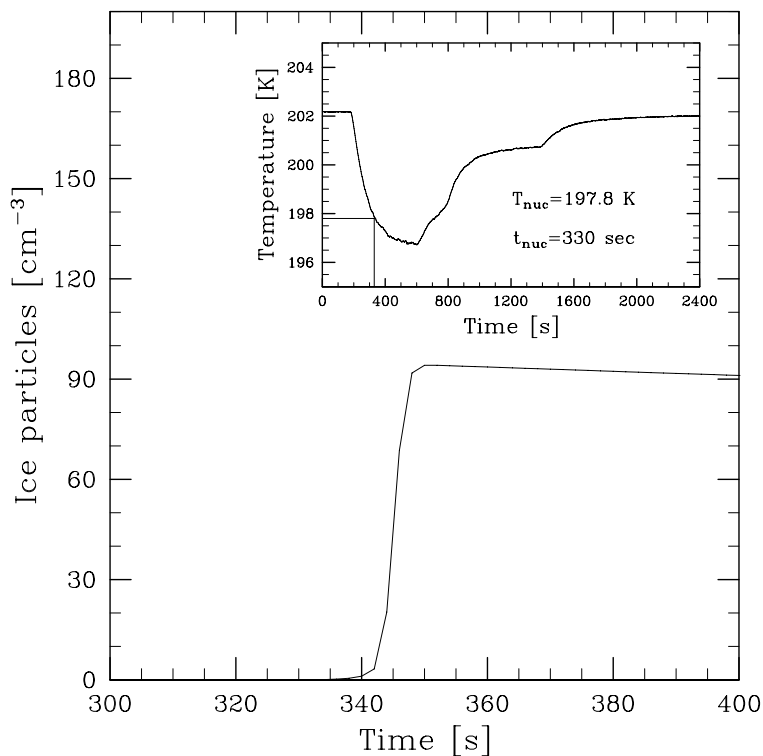
Fig. 6. Modeled number density of ice particles versus time. Per definition, the onset of freezing is found at 330 sec, the time when the concentration of ice particles exceeds $10^{-3}\,\mathrm{cm}^{-3}$ (not visible). The corresponding freezing temperature is $T_{\mathrm{nuc}} = 197.8\,\mathrm{K}$.

© EGU 2002
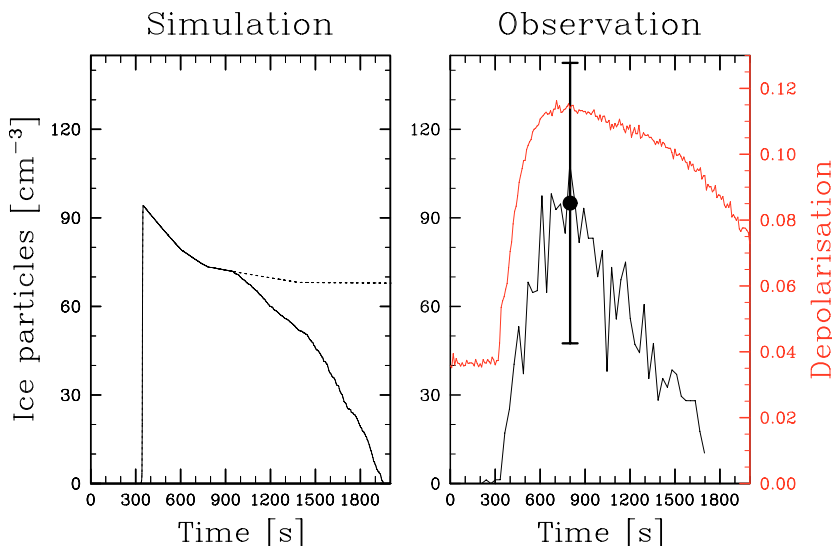
Fig. 7. Total ice particle number densities versus time (modeled values on the left panel, measured values on the right panel). The simulation shows two results with and without loss of ice water caused by sedimentation, wall impaction, or undersampling of large ice particles (solid and dashed curve, respectively). The vertical bar depicts the experimental uncertainty in measuring ice number densities. The red curve depicts the measured depolarisation signal detected with an Argon laser, ascribed to the formation and growth of ice particles.

Fig. 8. Modeled aerosol number size distributions (top panel) and ice particles number size distributions (bottom panel) around the time of ice nucleation. The color coding displays the simulation time advancing in steps of 10 s. The dotted curve in the top panel is the initial aerosol size distribution.

Fig. 9. Modeled size-resolved H_2O mass fractions of the H_2SO_4/H_2O droplets around the time of ice nucleation. The dotted line shows the initial aerosol water content before cooling.

Fig. 10. Modeled partitioning of H_2O. The total mixing ratio is constrained by the FISH measurements, while the gas phase, aerosol phase, and ice phase water mixing ratios are computed by the APSC model with (solid curves) or without (dotted curves) the effects of ice water losses after 900 s.
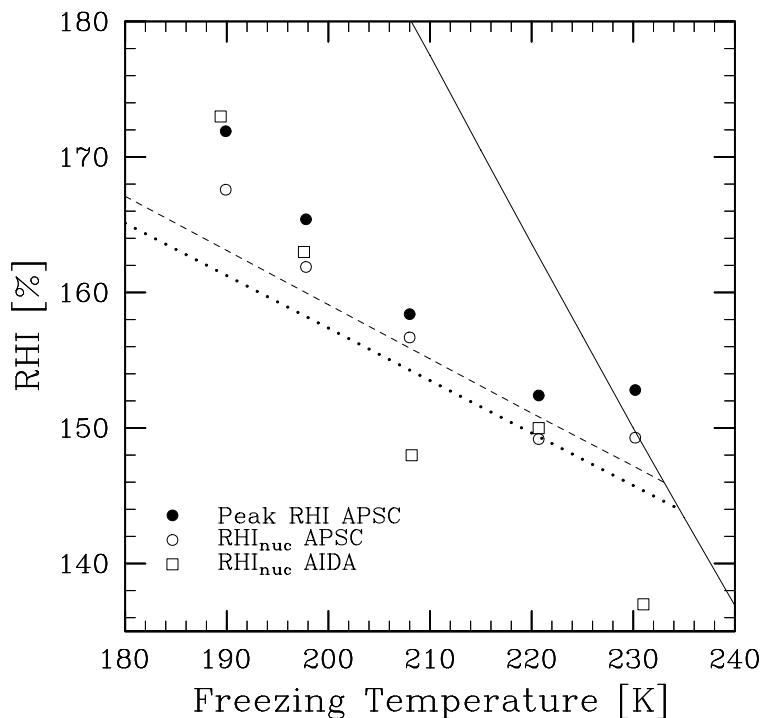
Fig. 11. Modeled baseline values of peak RHI and RHI$_{nuc}$ (closed and open circles) and measured threshold values for homogeneous ice nucleation inside the AIDA chamber (squares). The solid line indicates RHI when liquid water is saturated. The dashed (dotted) line depicts RHI$_{nuc}$ for which a particle with radius 0.25 (1) μm freezes homogeneously in one second (minute) (Koop et al., 2000). The experimental uncertainty of RHI$_{nuc}$ ranges from ±5% at 230 K to ±12% at 190 K (Möhler et al., 2002).

Title Page

Abstract · Introduction

Conclusions · References

Tables · Figures

◄◄ · ►►

◄ · ►

Back · Close

Full Screen / Esc

Print Version

Interactive Discussion

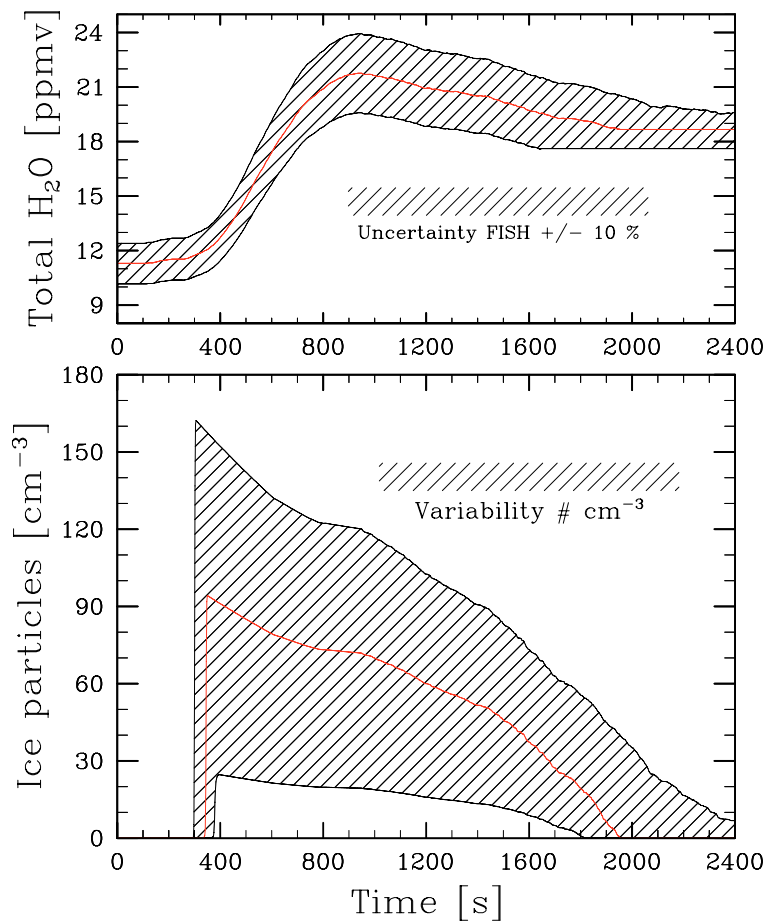**Numerical simulations of homogeneous freezing**

Haag et al.

Fig. 12. Variation of the modeled ice number density caused by imposed shifts of the FISH data by ± 10%. The red line indicates the baseline model run discussed in Sect. 4.
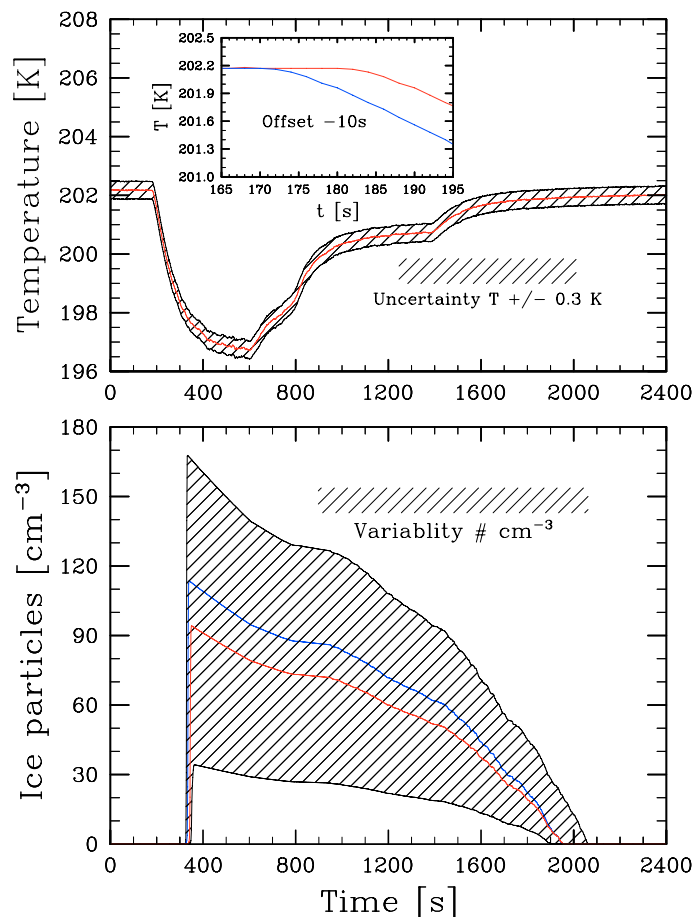
Fig. 13. Variation of the modeled ice number density caused by imposed shifts of the temperature data by ± 0.3 K (top panel) and by a shift of the time axis by −10 s (bottom panel). The red curve indicates the baseline model run discussed in Sect. 4; the blue curve representing the shifted profile is not visible on the extended scale in the top panel.

Numerical simulations of homogeneous freezing

Haag et al.

Title Page

Abstract | Introduction

Conclusions | References

Tables | Figures

◄◄ | ►►

◄ | ►

Back | Close

Full Screen / Esc

Print Version

Interactive Discussion